# Core-shell carbon-polymer quantum dot passivation for near infrared perovskite light emitting diodes

Marinos Tountas,[1,2] Anastasia Soultati,[1] Konstantina-Kalliopi Armadorou,[1] Kalliopi Ladomenou,[3] Georgios Landrou,[3] Apostolis Verykios,[1] Maria-Christina Skoulikidou,[1] Stylianos Panagiotakis,[1] Petros-Panagis Fillipatos,[1,4] Konstantina Yannakopoulou,[1] Alexander Chroneos,[5,6,*] Leonidas C. Palilis,[7] Abd. Rashid Bin Mohd Yusoff,[8] Athanassios G. Coutsolelos,[3,*] Panagiotis Argitis,[1] Maria Vasilopoulou[1,*]

[1]Institute of Nanoscience and Nanotechnology, National Center for Scientific Research Demokritos, Agia Paraskevi, 15341 Athens, Greece

[2]Department of Electrical & Computer Engineering, Hellenic Mediterranean University, Estavromenos, Heraklion, GR-71410, Crete, Greece

[3]Department of Chemistry, University of Crete, Laboratory of Bioinorganic Chemistry, Voutes Campus, Heraklion 70013, Crete, Greece

[4] Faculty of Engineering, Environment and Computing, Coventry University, Priory Street, Coventry CV1 5FB, United Kingdom

[5]Department of Materials, Imperial College, London SW7 2AZ, United Kingdom

[6]Department of Electrical and Computer Engineering, University of Thessaly, 38221 Volos, Greece

[7]Department of Physics, University of Patras, 26 504, Rio, Greece

[8]Department of Chemical Engineering, Pohang University of Science and Technology (POSTECH), Pohang, Gyeongbuk 37673, Republic of Korea

## Abstract

High-performance perovskite light-emitting diodes (PeLEDs) require a high quality perovskite emitter and appropriate charge transport layers to facilitate charge injection and transport within the device. Solution-processed n-type metal oxides represent a judicious choice for the electron transport layer (ETL); however, they don't always present surface properties and energetics compatible with the perovskite emitter. Moreover, the emitter itself exhibits poor nanomorphology and defect traps that compromise the device performance. Here, we modulate the surface properties and interface energetics between the tin oxide ($SnO_2$) ETL with the perovskite emitter by using an amino functionalized difluoro{2-[1-(3,5-dimethyl-2*H*-pyrrol-2-ylidene-*N*)ethyl]-3,5-dimethyl-1*H*-pyrrolato-*N*}boron (BDP) compound and passivate the defects present in the perovskite matrix with carbon-polymer core-

shell quantum dots (PCDs) inserted into the perovskite precursor. Both these approaches synergistically improve the perovskite layer nanomorphology and enhance the radiative recombination. These properties resulted in the fabrication of near-infrared (NIR) PeLEDs based on formamidinium lead iodide ($FAPbI_3$) with a high radiance of 92 W $sr^{-1}$ $m^{-2}$, an external quantum efficiency (EQE) of 14%, reduced efficiency roll-off and prologned lifetime. In particular, the modified device retained 80% of the initial EQE ($T_{80}$) for 33h compared to 6h of the reference cell.

## 1. Introduction

Metal halide perovskite emitters offer significant advantages such as easy tuning of their bandgap through compositional engineering and size tuning in the case of nanocrystals, photoluminescence quantum yields (PLQY) close to unity across a broad range of emission colors and symmetrical narrow emission spectra [1-4]. Thanks to these properties, it is anticipated that they can be suitable candidates for light emitting diodes with tunable color emission ranging from ultra-violet to the NIR region [5-7]. Despite the remarkable progress shown by light-emitting diodes based on perovskites (PeLEDs) with EQEs recently exceeding 23% [8,9], significant challenges remain unsolved, including inability to access long wavelength (>1000 nm) emission, significant efficiency roll-off and short lifetime [10-12]. Optimizing the properties of the perovskite layer and the interfaces is of vital importance in order to achieve efficient and stable devices.

Modulation of the perovskite nanomorphology is imperative in order to enhance the performance of these devices. For example, three-dimensional (3D) perovskite emitters exhibit fast electron-hole dissociation, which decreases the probability of radiative recombination events. Strategies pursuing the confinement of charge carriers through reduction in the grain size can alleviate this issue [13-16]. In addition, the incorporation of passivation agents into the precursor solution can also modify the resultant perovskite film morphology, while also passivate defects that act as non-radiative recombination centers [17,18]. Effective passivation materials such as amino-acid additives can coordinate to undercoordinated $Pb^{2+}$ or halide ions or form ionic bonding to neutralize charged defects [19]; thus improving the device performance [20]. Additionally, carbon quantum dots with different functional groups have been used to passivate the perovskite methyl ammonium lead iodide ($CH_3NH_3PbI_3$) surface for application in photovoltaics [21]. Dependent on the ligand, this passivation approach either modified the crystal size or decreased the defect density in the perovskite film, thereby promoting efficiency enhancement.

Solution-processed inorganic metal oxides, such as aluminum-doped zinc oxide (AZO) and $SnO_2$ are common ETLs for efficient PeLEDs [22-24]. These materials exhibit adequated n-type conductivity combined with wide bandgaps, thus affording a high transparency within the visible

spectrum, a suitable conduction band minimum to match with that of the perovskite emitter and a deep valence band maximum to afford efficient hole blocking [25]. However, a common issue is their poor interface quality with the perovskite, which can be dentrimental to the device performance [26]. This issue can be overcome with appropriate surface treatment or interface modification [26-28].

Here, we optimize the structural, morphological and optoelectronic properties of a $FAPbI_3$ perovskite emitter through adopting a PCD additive engineering approach. We also modify the surface properties of $SnO_2$ ETL by coverage with an amino-functionalized BDP. The additive engineering changes the perovskite microstructure and film nanomorphology and reduces non-radiative recombination. The BDP surface modifier on the ETL reduces the electron injection barrier and modulates the surface energy hence altering the perovskite microstructure and film nanomorphology. This synergistic approach enabled the fabrication of NIR PeLEDs (peak emission at 780 nm) with a high radiance of 92 W $sr^{-1}$ $m^{-2}$ and EQE of 14%, representing a large improvement compared to the reference device (2.5 W sr-1 $m^{-2}$ and 6%). These devices also exhibited reduced efficiency roll-off and prolonged $T_{80}$ lifetime compared to the reference ones.

## 2. Experimental section

**Perovskite precursor preparation.** 27.7-mg formamidinium iodide (FAI) purchased from GreatCell Solar, 33.2-mg lead iodide ($PbI_2$) obtained from Sigma-Aldrich, and 7.7-mg 5-aminovaleric acid (AVA) purchased from Sigma-Aldrich dissolved in 1 ml of anhydrous N,N-dimethylformamide (DMF) (Sigma-Aldrich). The precursor solution was stirred for 2 h at 80 °C in an argon-filled glove box before use.

**PeLED fabrication and characterization.** Patterned indium-tin oxide (ITO) coated glass substrates with sheet resistance 8 Ω/square (Ossila) were used for PeLEDs fabrication. The substrates were cleaned in deionized (DI) water, acetone, and 2-propanol, for 10 min and dried with $N_2$ before they further treated by UV-ozone for 20 min. A solution of colloidal dispersion of tin(IV) oxide in deionized water (15%, Alfa Aesar) was spin-coated on ITO substrates at 3000 rpm for 30 seconds. The $SnO_2$ films annealed at 150 ºC for 30 minutes. For the BDP modified $SnO_2$ films, a solution of 0.5 mg $mL^{-1}$ in chlorobenzene (CB) was spin-coated at 2000 rpm for 40 seconds atop $SnO_2$ film. The perovskite precursor solution was spin-coated at 3000 rpm for 1 min, followed by annealing at 100 °C for 16 min. As the hole transport layer (HTL), poly-TPD (poly(N,N′-bis(4- butylphenyl)-N,N′-bisphenylbenzidine, Sigma Aldrich) was spin-coated from chlorobenzene solution (13 mg $ml^{-1}$). Molybdenum oxide ($MoO_3$, 10 nm) and aluminum (Al) were thermally evaporated to serve as the hole injection layer and anode electrode, respectively. For the device characterization, the current density-

voltage-luminance (J-V-L) curves, radiance, and EQE were all carried out with an Oriel spectrometer coupled with a fiber integration sphere (FOIS-1) and a Keithley 2400 source meter.

**Characterization methods.** Fourier-transform infrared (FT-IR) spectroscopy was performed using a Bruker Tensor 27 spectrophotometer with a DTGS detector. $^{1}$H NMR spectra were recorded on a Bruker Avance 500 MHz spectrometer as solutions in deuterated DMSO-$d_6$ using the residual solvent signal as the internal standard and were processed with Topspin 4.0.8. X-ray photoelectron spectrum (XPS) was recorded by a Leybold EA-11 electron analyzer operating in constant energy mode at a pass energy of 100 eV. The X-ray source was a nonmonochromatized Al K line at 1486.6 eV (12 keV with 20 mA anode current). The work function ($W_F$) of pristine and BDP-modified $SnO_2$ films were estimated after recording the ultraviolent photoemission spectra (UPS) of the films deposited on ITO substrates used for PeLEDs fabrication. For the UPS measurements, the He I (21.22 eV) excitation line was used and a negative bias of 12.28 V was applied to the sample in order to separate sample and analyzer high binding energy cut-offs and estimate the absolute work function value. Atomic Force Microscopy (AFM) images were captured using an XE7 microscope (Park Systems) by operating in tapping mode. The crystallinity of perovskite films was investigated using an X-ray Siemens D-500 606 diffractometer. UV-Vis absorption spectra of the polymer solutions (concentration $10^{-5}$ M) and the prepared films were recorded with a Shimadzu UV-1900 spectrometer. Steady-state photoluminescence (PL) measurements were performed with a commercial platform (ARKEO - Cicci Research): the substrate was illuminated with a diode-pumped solid-state (DPSS) Nd:YVO4+KTP Laser (peak wavelength 532 nm ± 1 nm, optical power 1 mW on a circular spot of 2 mm of diameter: 31 mW cm$^{-2}$) at an inclination of 45°. The fluorescence on the opposite side of the substrate is focused on a bundle of fibers (10 mm in diameter) with an aspheric lens close to the substrate to maximize the PL. The bundle sends the signal to a CCD-based spectrometer. Integration time and the number of averaging was maintained the same to better compare the results. Time-resolved photoluminescence (TRPL) spectra were measured with an FS5 Spectrofluorometer from Edinburgh Instruments. A 478.4nm laser was used as an excitation source. SEM images of the perovskite films were recorded with a JEOL 7401f FESEM.

## 3. Results and Discussion

### 3.1 Preparation of core-shell carbon-polymer quantum dots (PCD).

The QDs used in this study were synthesized through a bottom-up hydrothermal method, according to Ladomenou et al. [30]. In brief, citric acid (CA) and ethylene diamine (EDA) were used as starting materials and were reacted in an autoclave, followed by heating at 180°C for 8 hours (Figure 1a). A purification step took place for the final isolation of the desired product. This method has been

previously reported to yield pure carbon quantum dots when heating above 200 ºC [31,32]; however, we intentionally applied here lower temperature during the synthesis in order to receive intermediate products with different degrees of polymerization [33]. We aimed to isolate shell-core polymer-carbon QDs having the molecule 5-oxo-1,2,3,5-tetrahydroimidazo[1,2-α]pyridine-7- carboxylic acid (IPCA) as the polymeric shell. The mixture or assembly IPCA-carbon dots (PCDs) was purified in a 1000 Da dialysis membrane and the fluorophore IPCA hasn't been removed, as shown in $^{1}$HNMR spectra (Figure 1b, S1). Figure 1b at red line presents a spectrum without starting materials, while the aliphatic protons of carbon cores at 4.2-2.5 ppm were overlapped with two characteristic aliphatic triplet peaks. Then, two characteristic of double bond peaks at 6.0-5.6 ppm conclude the present of IPCA in carbon dots solution. Many differences between PCDs and simple carbon dots produced from citric acid were observed (Figure S2).

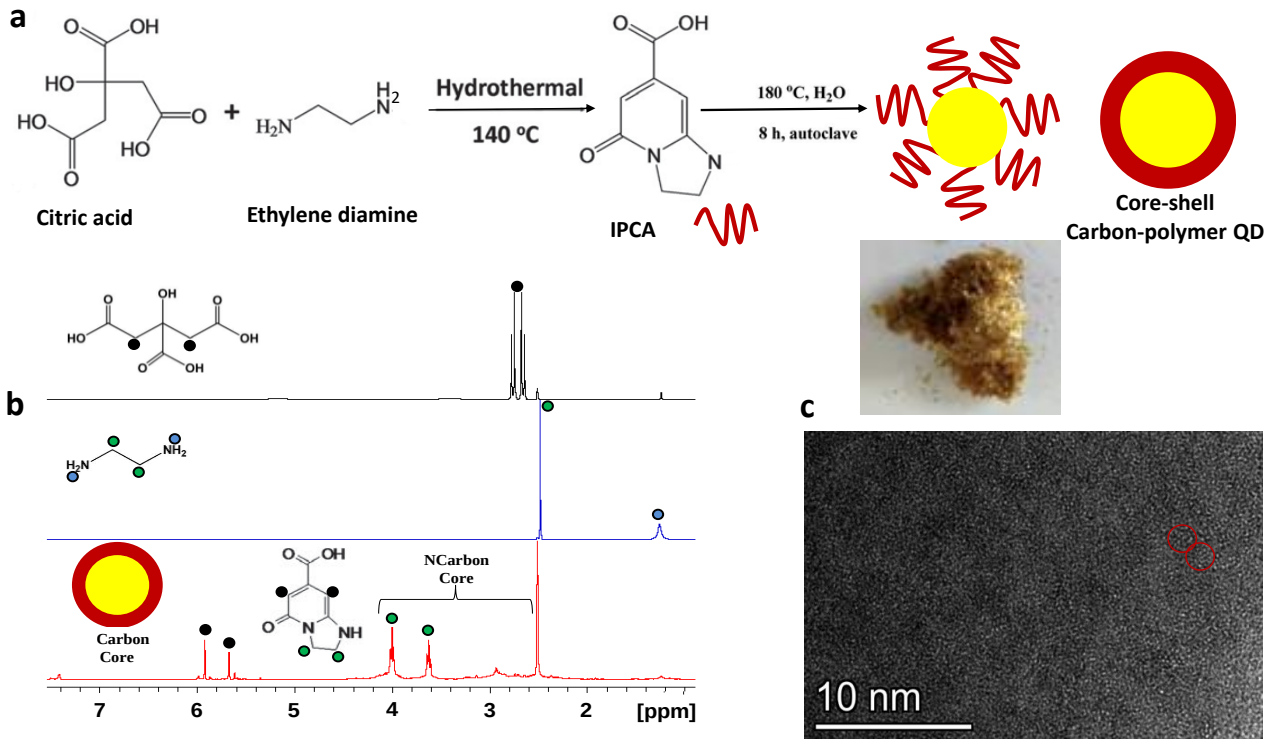


**Figure 1.** (a) Synthetic procedure for the preparation of core-shell carbon-polymer (PCD) quantum dots. (b) $^{1}$H NMR spectra of CA, EDA and PCD and (c) high resolution TEM image of the synthesized quantum dots. Only the carbon core is clearly seen in this picture.

The existence of carbon core in the PCDs is evident by the transmission electron microscopy (TEM) measurements, presented in Figure 1c. We can conclude that the product contains a carbon core with a diameter of around 2.5 nm. The existence of an extensive amine network in the polymeric shell of these dots is expected to offer bulk and surface passivation in the perovskite through effective coordination with undercoordinated lead cations ($Pb^{2+}$), which will benefit the device performance and stability.

### 3.2 Surface modification of $SnO_2$ using amino BODIPY.

Besides the emissive layer, the charge injection/transport and interlayer materials also play a crucial role in the device performance, as they dictate efficient charge injection and transport within the device layers and heterointerfaces; they can also modify the nanomorphology of the perovskite emitter deposited atop. Therefore, we first investigated the optoelectronic and structural properties of $SnO_2$ as-deposited and coated with a very thin BDP interlayer (from a 0.5 mg $mL^{-1}$ solution in CB).

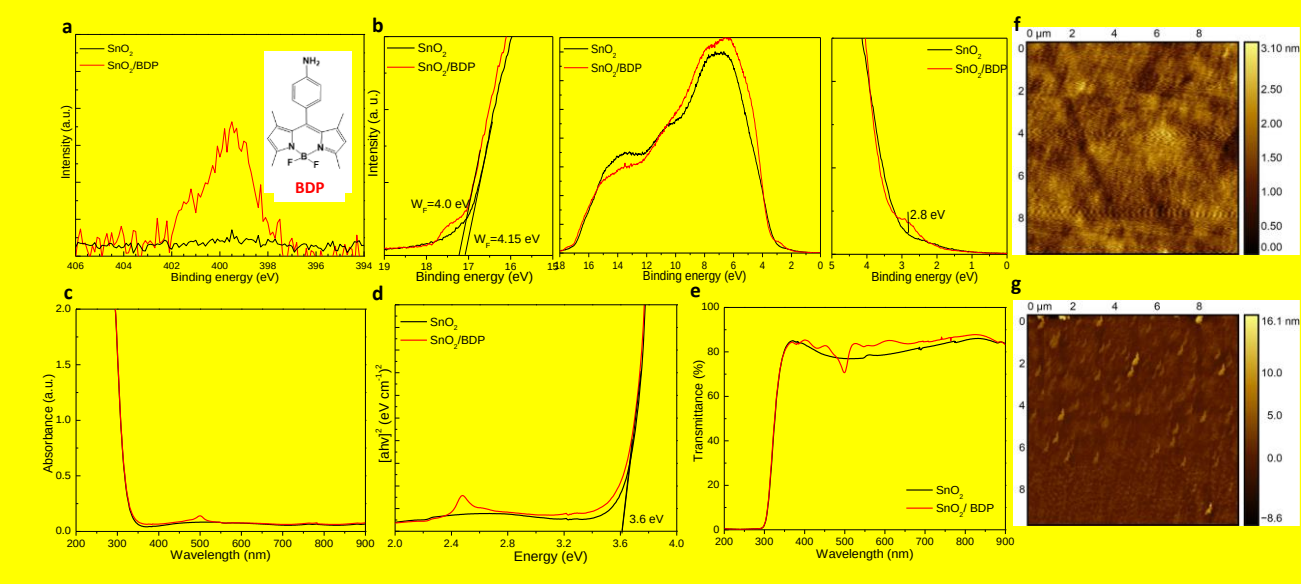


**Figure 2.** (a) N 1s core level peaks of a $SnO_2$ and $SnO_2$/BDP layers. The chemical structure of amino BDP is shown as inset. (b) UPS spectra of $SnO_2$ and $SnO_2$/BDP films: the high binding energy cut-off (left), the UPS spectra (middle) and the near Fermi level region (right) of the UPS spectra of the prepared samples. (c) UV-Vis absorption spectra, (d) the Tauc plots derived from absorption measurements and (e) transmittance spectra of $SnO_2$ and $SnO_2$/BDP layers on glass/ITO substrates. 10 x 10 $\mu m^2$ AFM surface topographic images of (f) $SnO_2$ and (g) $SnO_2$/BDP films.

The formation of a thin BDP interlayer on top of $SnO_2$ is evidenced by the X-ray photoelectron spectroscopy (XPS) measurements, which showed the existence of nitrogen (N) in the BDP covered oxide (termed as the $SnO_2$/BDP sample). Figure 2a shows the N1s core level peaks of the XPS spectra taken in pristine $SnO_2$ and BDP/$SnO_2$ [34]. We observe that this BDP has covered the surface of $SnO_2$ having as a result a surface work function ($W_F$) reduction. From the shift towards higher binding energy (BE) in the electron cut-off of the ultra-violet photoelectron spectroscopy (UPS) measurements of BDP/$SnO_2$ (Figure 2b), a $W_F$ reduction of 150 meV (from 4.15 eV to 4.0 eV) is concluded. This shift is due to the formation of a negative interfacial dipole arising from the amino groups, which push electrons toward the $SnO_2$ and effectively reduce its surface $W_F$ [35,36]. This is expected to improve electron injection towards the conduction band of the perovskite emitter [37].

On the other hand, a characteristic peak appears near the onset of the valence band, in particular, at around 2.8 eV, in the UPS spectrum of BDP/$SnO_2$. This peak can be attributed to BDP as evidenced by the UPS spectrum of a pristine BDP layer coated (from a 5 mg $mL^{-1}$ solution in CB) on ITO/glass (Figure S3). Figure 2c,d and e show the UV-Vis absorption, the derived Tauc plots and transmittance spectra of $SnO_2$ as-deposited and coated with BDP. Whereas the presence of BDP is evident by the characteristics absorption peak at around 500 nm (Figure S4), it does not alter significantly the transmittance spectrum of the transparent bottom electrode. In addition, the energy bandgap value ($E_g$) was calculated from the Tauc plots to be 3.6 eV in both cases.

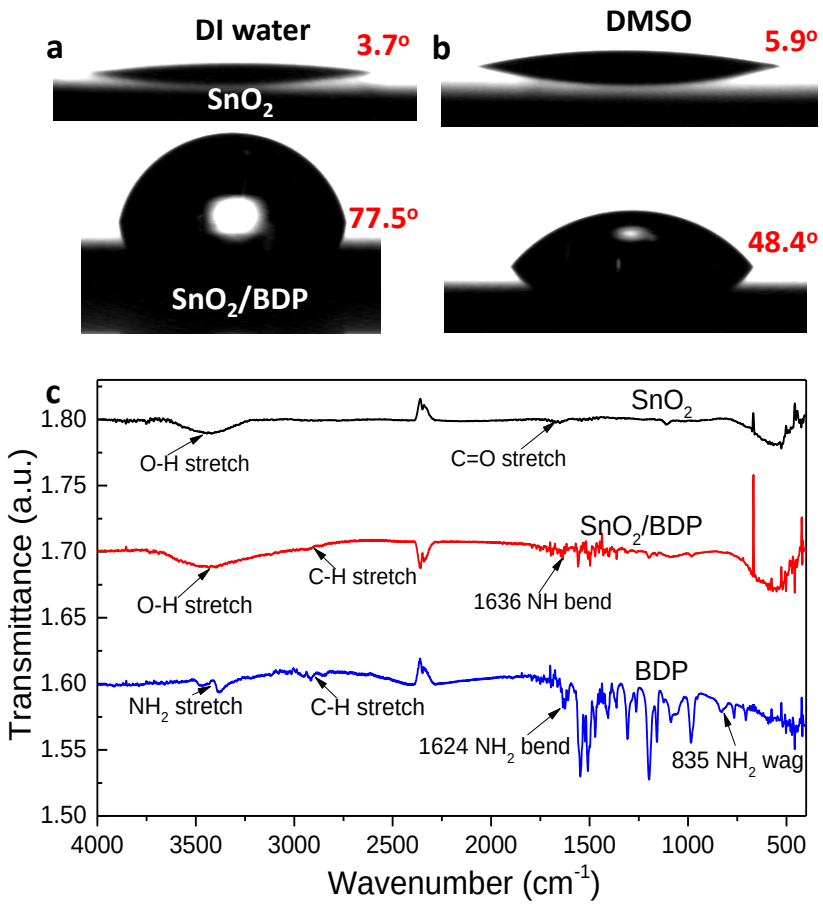


**Figure 3.** Contact angle measurements taken on a pristine $SnO_2$ (top) and $SnO_2$/BDP substrate (bottom) for a droplet of (a) water and (b) DMSO. (c) FT-IR spectra of pristine $SnO_2$ and BDP films and of a $SnO_2$/BDP layer.

The surface topography of $SnO_2$ before and after the BDP coverage was further investigated with atomic force microscopy (AFM) measurements. Figure f and g show the surface topographies of as-deposited and BDP-modified $SnO_2$, respectively, where it is seen that the BDP modifier has covered the surface of $SnO_2$. The root-mean-square (RMS) surface roughness slightly increased from 0.35 to 1.14 nm, which is not expected to significantly alter the perovskite overlayer. Interestingly, the BDP-modified $SnO_2$ exhibited significant differences in water contact angle (Figure 3a) and adhesion in

DMSO solvent (Figure 3b), with respect to the pristine $SnO_2$ substrate. In particular, the pristine oxide surface exhibits high hydrophilicity due to the high amount of hydroxyl groups present on the oxide's surface. This, however, has been proven detrimental for the device operation as these negative hydroxyl groups may attract positively charged ions within the perovskite layer [38]. A layer of such positive ions may thus built-up at the respective interface hence upward shifting the vacuum level and increasing the electron injection barrier.

Fourier-transform infrared (FT-IR) measurements were performed for the $SnO_2$ thin film, BDP thin film and BDP coated on top of $SnO_2$ (Figure 3c). In the FT-IR spectrum of BDP, the bending modes of N-H can be detected at 1624 $cm^{-1}$ whereas the stretching modes appear at around 3500 $cm^{-1}$. The characteristic stretching band of $SnO_2$ made by the vibrations of the Sn–O–Sn bond is centered at 640 $cm^{-1}$. However, tin oxide exhibits a strong broad peak in the 3630-3220 $cm^{-1}$ area; this is the characteristic stretching band of hydroxyl group (O-H stretching). This band also appears centered around 3430 $cm^{-1}$ in the $SnO_2$/BDP spectrum but with lower intensity. One possible explanation of this is that in the pure $SnO_2$ film, the surface is rich with hydroxyl groups and with the addition of BDP these groups form extensive hydrogen bond networks with the $-NH_2$ groups of BDP thus being inactivated. As a result, reduced hydrophilicity is obtained for the BDP modified oxide surface, which increases the surface tension and also the measured contact angle for a DMSO droplet. We expect that this will directly influence the nanomorphology of the perovskite overlayer.

To gain an insight into the effect of the $SnO_2$ surface modification on the structural properties and crystallinity of the perovskite film coated atop, X-ray diffraction (XRD) measurements were performed. Figure 4a and b presents the XRD patterns of $FAPbI_3$ films (without AVA) spin-coated on $SnO_2$ without and with BDP surface modification, respectively. It becomes evident that the characteristic perovskite peaks are more pronounced in the $SnO_2$/BDP/$FAPbI_3$ sample. More interestingly, the full-width-half-maximum (FWHM) of the crystallization peak at ~13.9° corresponding to the (001) plane is reduced indicating improved film quality with low roughness and smaller overall crystal size of 48.78 nm compared with the 56.57 nm for the $FAPbI_3$ spin-coated on the pristine $SnO_2$. Furthermore, the increased intensity of the same (001) crystallization peak also suggests that the surface modifier of $SnO_2$ enhances the preferred orientation of the perovskite film deposited on top and suppresses the formation of $PbI_2$.

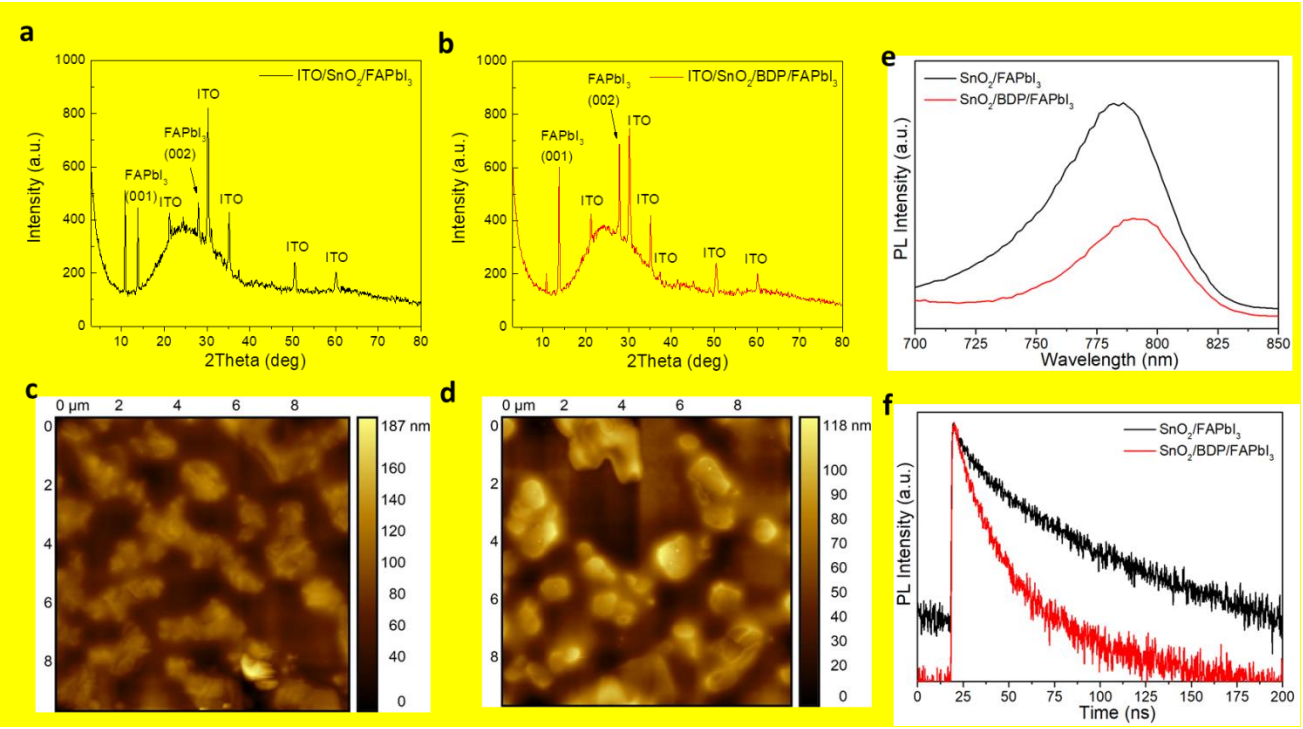


**Figure 4.** XRD patterns of $FAPbI_3$ films deposited on (a) $SnO_2$ and (b) $SnO_2$/BDP layers. 10x10 $\mu m^2$ AFM surface topography of $FAPbI_3$ perovskite deposited on (c) pristine and (d) surface modified with BDP $SnO_2$ electron transport layer. (e) Steady-state photoluminescence (PL) spectra and (f) transient photoluminescence (TRPL) decay curves of $FAPbI_3$ perovskite deposited on pristine and BDP modified $SnO_2$ layer.

The nanomorphology of $FAPbI_3$ perovskite was also altered when coated onto the BDP modified $SnO_2$. AFM 10x10 $\mu m^2$ topographies of a 50 nm thick $FAPbI_3$ deposited on pristine and BDP-modified $SnO_2$ on glass/ITO substrates are shown in Figure 4c and d, respectively. In the reference sample, interconnecting grains are observed, which form a "network" of long perovskite islands. However, in the case of perovskite deposited directly onto BDP, these grains are smaller and separated one from the other. The same conclusion can be drawn from scanning electron microscopy (SEM) topographic images of the same samples (Figure S5). This can be explained by taking into account the reduced hydrophilicity of the BDP-coated $SnO_2$ sample. In hydrophilic surfaces water molecules adsorbed onto them act as nucleation sites for the perovskite formation. As a result, extended perovskite grains are formed in hydrophilic surfaces which are highly desired for perovskite solar cells [38]. However, the situation is different for perovskite LEDs where smaller grains are necessary in order to confine both charges and excitons and increase the radiative recombination rate [39]. We therefore argue that the decrease in grain size in the perovskite coated onto the BDP modified substrate could be beneficial for LED operation [40]. Additionally, a reduction in surface roughness of the perovskite film deposited onto the BDP-modified ETL (from 22.48 nm for the reference sample

$SnO_2$/$FAPbI_3$ to the 19.51 nm for the $FAPbI_3$ deposited on $SnO_2$/BDP) is indicative of a better contact quality between the perovskite emitter and the hole transport layer deposited on top of it.

Moreover, the interfacial electron transport between the perovskite and $SnO_2$ in the absence and presence of the BDP surface modifier was studied by using steady-state photoluminescence (PL) and transient PL (TRPL) measurements. As shown in Figure 4e, the $FAPbI_3$ coated on the ITO/$SnO_2$/BDP substrate exhibits a 44% reduction in the PL intensity, indicating a faster electron extraction from the perovskite to the metal oxide, which can be due to a reduction in the electron injection/extraction barrier at the interface. This indicates that enhanced electron injection can also be obtained upon the application of a forward bias during the device operation. The same conclusion can be drawn from the decrease in carrier lifetime shown in transient PL (TRPL) spectra of Figure 4f. A red shift of about 10 nm the PL peak is also observed for the BDP/$FAPbI_3$ sample, which can be attributed to changes in the lattice parameters; in particular, a small shift from 13.89º to 13.83º for the (001) XRD peak of BDP/$FAPbI_3$ is also observed. These changes may originate from coordination of the amino groups of the BDP underlayer with undercoordinated $I^-$ or $Pb^{2+}$ within the perovskite lattice resulting in trap filling and better interface quality. Notably, the absorption spectra of the two samples were nearly similar (Figure S6).

### 3.3 Core-shell carbon polymer dots as perovskite additives

To passivate defects present in the perovskite bulk, we next applied core-shell carbon-polymer quantum dots (PCD) as the passivation agent embedded into the $FAPbI_3$ perovskite emitter. We first tested their effect in the perovskite microstructure (without AVA) and the nanomorphology of the resultant perovskite layer (without AVA). Figure 5a and b shows the scanning electron microscopy (SEM) images of the perovskite derived from the spin coating (onto glass/ITO substrates) of the precursor solution without and with PCDs (in a concentration of 1 mg $mL^{-1}$ in the precursor). It becomes evident that PCDs largely affect the layer morphology resulting in the formation of well-defined nanograins of smaller size compared to the reference sample which consists of longer perovskite “islands”. These small grains can strongly confine excitons and charges therein thus increasing the radiative recombination, which is crucial for perovskites that generally exhibit low exciton binding energies of few meV [41]. These grains are slightly decreased in size when coated on top of the BDP layer. Figure 6 a-d depicts the AFM topographies of $FAPbI_3$ films embedding PCD additive in a concentration of 0.4mg $mL^{-1}$ and 1mg $mL^{-1}$ (named hereafter as $FAPbI_3$+PCD-0.4 and $FAPbI_3$+PCD-1, respectively) on top of pristine $SnO_2$ (Figure 6a and b, respectively) and on BDP-modified $SnO_2$ substrate (Figure 6c and d, respectively). It becomes evident that both layers, $FAPbI_3$+PCD-0.4 and $FAPbI_3$+PCD-1, consist of smaller grains when deposited on the BDP modified

$SnO_2$ exactly as in the case of pristine perovskite coated on as-deposited and BDP-modified oxides. Additionally, the $FAPbI_3$+PCD layers deposited on the $SnO_2$/BDP exhibited lower root-mean-square (RMS) surface roughness compared with the perovskite film coated on the pristine $SnO_2$. Especially, in the case of the $FAPbI_3$+PCD with concentration of 1mg $mL^{-1}$, the RMS was 14.5nm, while the $SnO_2$/$FAPbI_3$+PCD-1 exhibited higher RMS of 23.3nm. This significant improvement in the microstructure of the perovskite embedding PCD and of the nanomorphology of the perovskite film deposited on BDP coated $SnO_2$ is expected to be beneficial for the device performance.

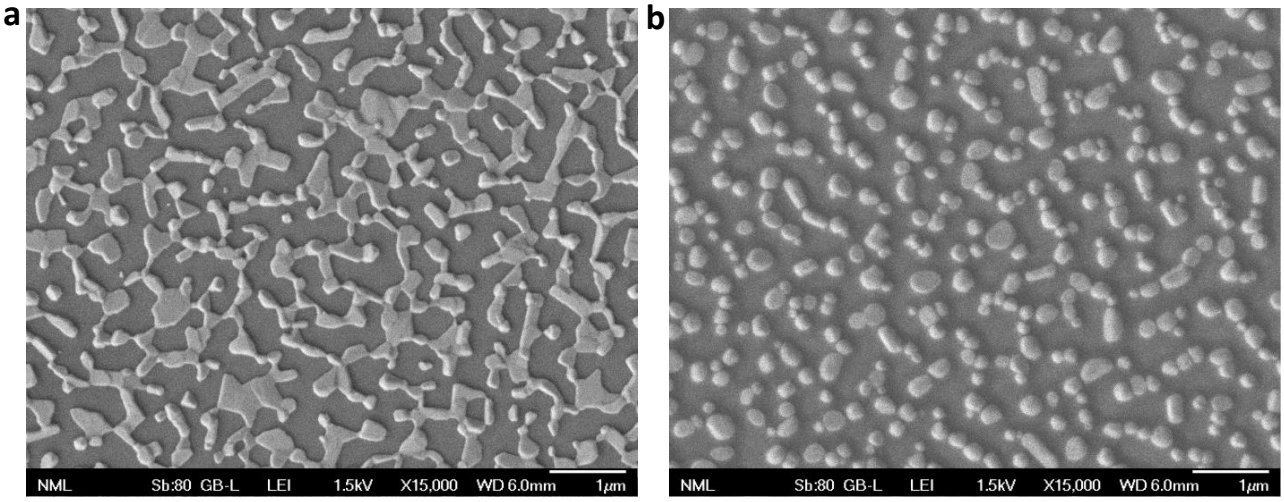


**Figure 5.** SEM images of a layer derived from (a) a pristine $FAPbI_3$ precursor (without AVA) and (b) the same precursor with PCD additive.

Furthermore, an increase in the intensity of the steady-state PL spectrum of the perovskite film (coated on glass) with a 0.4% concentration in PCDs compared to the reference film indicates the passivation effect of the polymerized carbon dots (Figure 6e). However, when inserted in a higher concentration these dots induce large decrease in the PL emission of the hybrid perovskite:carbon dot film. Notably, the UV-Vis absorption spectra of all samples were very similar (Figure S7). The same conclusions can be drawn from TRPL decay curves (Figure 6f) that also suggest a passivation effect of PCD with the lower concentration (i.e. 0.4 mg $mL^{-1}$). PL and TRPL measurements taken in perovskite samples without and with the carbon dots coated on as-deposited and BDP-modified SnO2 also indicated enhanced charge injection, when using the BDP interlayer, as well as, the passivation effect of PCDs (Figure S8).

### 3.4 Perovskite LED performance

PeLEDs based on $FAPbI_3$ perovskite emissive layers with and without PCD additive (0.4 mg $mL^{-1}$) using pristine $SnO_2$ or BDP-modified $SnO_2$ were next fabricated. They consisted of the following layers: glass/ ITO (100 nm)/ $SnO_2$ or BDP-modified $SnO_2$ (40 nm)/ $FAPbI_3$ (+AVA)+PCD (50 nm)/

Poly-TPD (40 nm)/ $MoO_3$ (30 nm)/Al (100 nm). The corresponding energy levels of each layer are shown in Figure 7a. By inserting the BDP modification interlayer on top of $SnO_2$, a perfect alignment between the highest occupied molecular orbital (HOMO) of the interlayer and the valence band (VB) of the perovskite occurs. The insertion of a thin BDP interlayer on top of $SnO_2$ is expected to enhance electron injection and transport within the device.

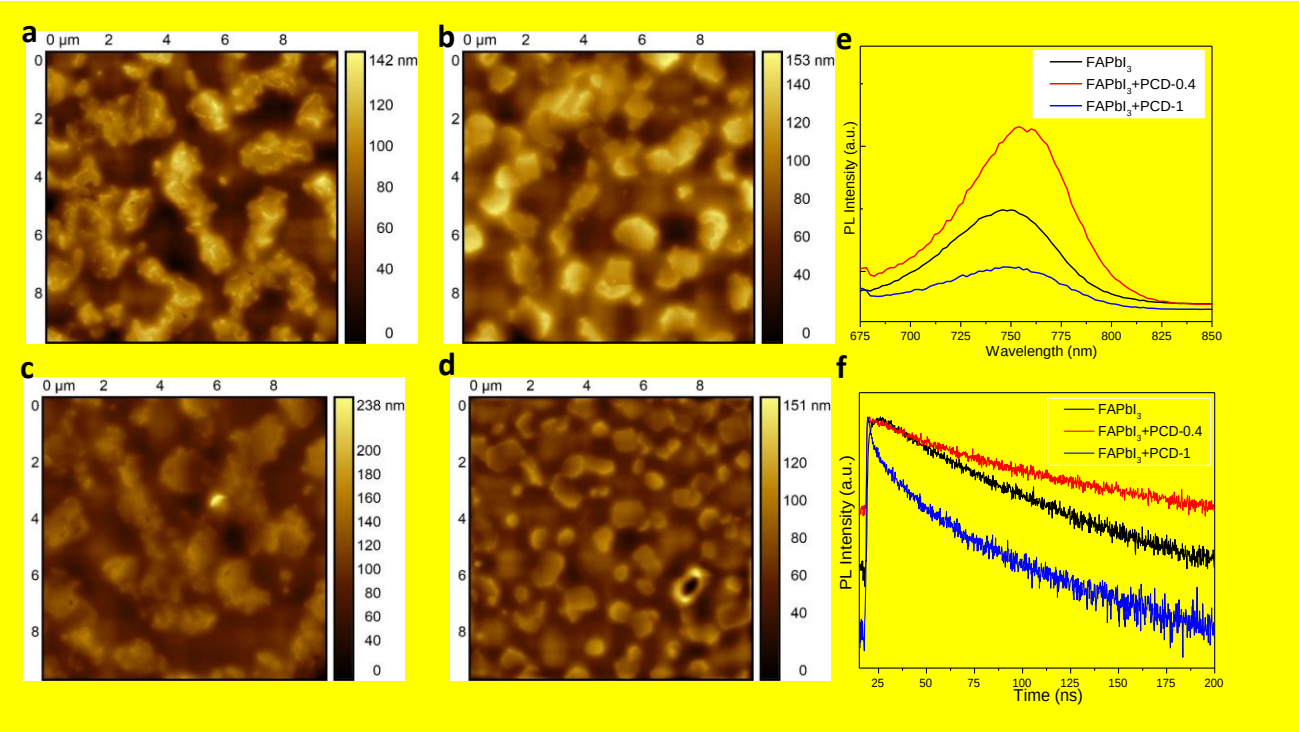


**Figure 6.** 10x10 $\mu m^2$ AFM surface topography of $FAPbI_3$ perovskite with two different concentrations of PCDs (0.4 mg $mL^{-1}$, a,c, and 1.0 mg $mL^{-1}$, b,d) deposited on pristine $SnO_2$ (a,b) and BDP coated $SnO_2$ (c,d). (e) Steady-state PL and (f) TRPL decay curves of $FAPbI_3$ perovskite with two different concentrations of PCDs deposited on glass.

Figure 7b shows the electroluminescence (EL) spectra of the pristine and modified with BDP $SnO_2$, combined with $FAPbI_3$ and $FAPbI_3$+PCD emissive layers. The devices showed a peak EL at 770 nm, which is blue shifted compared to the PL maxima (Figure S8). There are several reasons that can explain the differences between the EL and PL spectra. Photoluminescence is mainly determined by the optical properties of the material, while the electroluminescence is determined by a number of factors such as the optical properties and physical structures of the optically active layers, the electrical properties of two conductive regions, which are used for cathode and anode contacts, and the properties of the electrical contacts through which the electrical current injected. Electroluminescence is usually performed on the finished devices (such as LEDs) since it needs a device structure to inject current. As LEDs are multilayer structures with thicknesses on the order of the emission wavelength, EL spectra will depend on both the thicknesses and the refractive indices of the individual layers as a result of interference effects in a "weak" microcavity [42]. The above parametes will influence the position

of the recombination zone hence affecting the profile and intensity of the EL spectrum. Furthermore, other phenomena such as suppression of Auger recombination under external bias has been reported to alter the profile of PL and EL spectra [43].

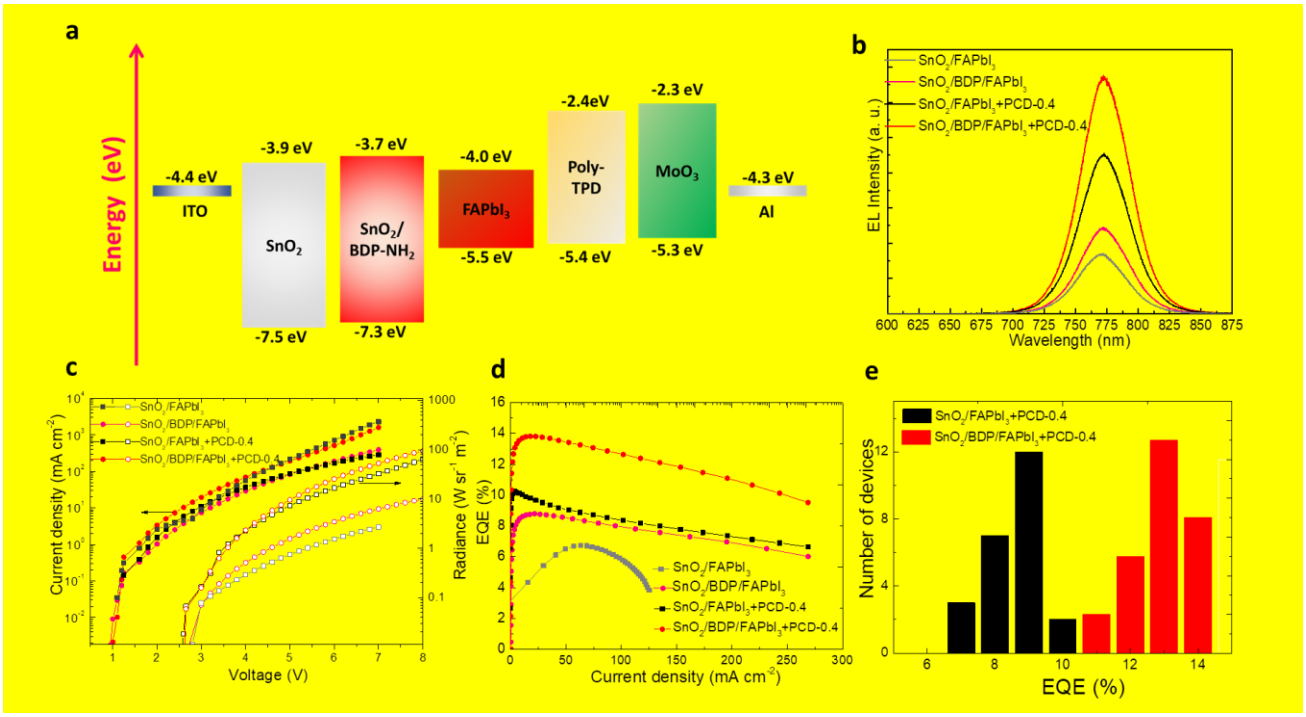


**Figure 7.** (a) Energy level alignment of different layers used in the device sequence considering vacuum level alignment before contact. (b) The electroluminescence spectra, (c) current density-voltage-radiance characteristics and (d) EQE plotted against the current density of the four types of the fabricated PeLEDs. (e) Device statistics extracted from a batch of 49 devices of each type.

The current density and radiance vs. voltage characteristics show that the devices using the BDP modified $SnO_2$ open at lower voltage compared to the reference ones (based on pristine $SnO_2$), which suggests efficient carrier injection from the modified bottom electrode (Figure 7c). More importantly, a large improvement in the radiance of the PCD-based PeLEDs was achieved. Especially, in the case of the device based on the $FAPbI_3$+PCD-0.4 coated on the BDP modifier the measured peak radiance was increased to 92 W $sr^{-1}$ $m^{-2}$, representing a large improvement compared to the reference device without PCDs and BDP (2.5 W sr-1 $m^{-2}$). The device with the $FAPbI_3$+PCD-0.4 emitter deposited on the pristine $SnO_2$ ETL showed also enhanced radiance of 54 W $sr^{-1}$ $m^{-2}$, indicating the beneficial role of the PCD on the device performance. Furthermore, a clear enhancement in the obtained EQE was found, when using the modified ETLs and the PCD PeLED emissive layers. EQE was measured to be 6% and 9% for the $FAPbI_3$ coated on the pristine and BDP modified $SnO_2$ ETL, respectively, which was increased to 10% and 14% for the PCD PeLEDs based on the $SnO_2$ and $SnO_2$/BDP substrates, respectively (Figure 7d). Table 1 provides a detailed comparison on the current advancement in the $FAPbI_3$ perovskites PeLEDs concluding the performance of our device and recent

state-of-the-art PeLEDs [44-55]. The optimized devices also showed reduced efficiency roll-off compared to the reference with no modification and additive (Figure 7d). They were also quite reproducible as shown by the histograms of the device EQE data extracted from a batch of for 49 devices (Figure 7e). The synergistic effect of our additive and interface engineering approach also resulted in enhanced device lifetime [56,57]. Figure 8 presents the variation of normalized EQE versus time of continuous operation of a reference PeLED (using $FAPbI_3$ and as-deposited $SnO_2$) and the optimized device based on $SnO_2$/BDP and PCD additive engineering approach. Both devices were biased at a current density of 50 mA $cm^{-2}$ (initial EQE of 6 and 13% for the reference and champion PeLED, respectively). The estimated $T_{80}$ lifetimes (the time where the EQE declines to 80% of the initial value) were 6 and 33 h for the reference and engineered device, respectively. This high performance and enhanced lifetime of the PCD PeLEDs is attributed to the passivation effect of PCD and the improved microstructure of the perovskite caused by the BDP and PCDs along with the favorable energy level alignment at the electron injection interface upon the BDP modification of $SnO_2$.

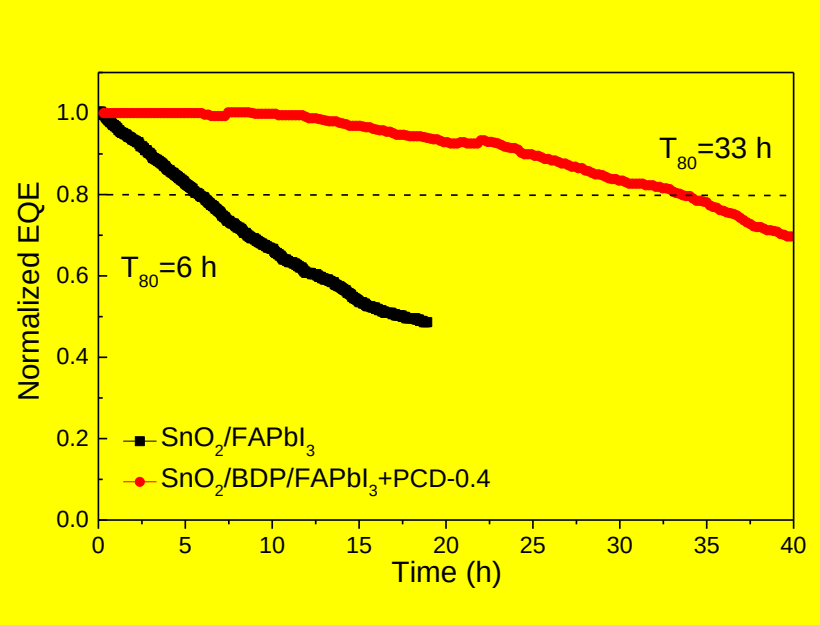


**Figure 8.** Variation of the normalized EQE of the reference PeLEDs using as-deposited $SnO_2$ and pristine $FAPbI_3$ (with AVA) layers and of the best performing device using BDP and PCDs.

## Conclusions

In conclusion, we have simoultaneously modified the surface of $SnO_2$ used as the bottom electron transport layer and the emissive layer in PeLEDs based on $FAPbI_3$. As a surface modifier for $SnO_2$, we used an amino-functionalized BDP, which alters the surface tension, as well as, the interface energetics thus favouring the formation of smaller perovskite domains and reducing the electron injection barrier simultaneously. We also inserted core-shell carbon-polymer quantum dots in the

perovskite emitter to passivate bulk defects and further alter the microstructure. As a result, the $FAPbI_3$ PeLEDs showed considerable performance enhancement, reduced efficiency roll-off and enhanced lifetime compared with the reference device without BDP and PCDs. This work suggests that surface modification of charge transport materials and additive engineering of the perovskite emitter represent vital solutions for further advancements in perovskite optoelectronics.

**Table 1.** Performance comparison of PeLEDs based on $FAPbI_3$ emissive perovskite layer.

| **Device structure** | **EQE (%)** | **Radiance (W $sr^{-1}$ $m^{-2}$)** | **Reference** |
|---|---|---|---|
| ITO/ZnO/PEIE/AAC-$FAPbI_3$/TFB/Au | 18 | 286 | 44 |
| ITO/ZnO/PEIE/EDEA-$FAPbI_3$/TFB/Au | 18 | 225 | 44 |
| ITO/ZnO/PEIE/ODEA-$FAPbI_3$/TFB/$MoO_3$/Au | 22.8 | 110 | 45 |
| ITO/ZnO/PEIE/$FAPbI_3$/TFB/$MoO_x$/Au | 19.9 | - | 46 |
| ITO/ZnO/PEIE/$BDAFA_{n-1}PbnI_{3n+1}$/TFB/ $MoO_3$/Au (n=6) | 4.7 | 148.9 | 47 |
| ITO/ZnO/PEIE/$FAPbI_3$/PMMA/TFB/$MoO_3$/Au | 19.6 | 875 (at 1500mA $cm^{-2}$) | 48 |
| ITO/PEDOT:PSS/TFB/PEF-$FAPbI_3$/TPBi/LiF/Al | 10.7 | 1.27 | 49 |
| Au/$MoO_3$/TFB/$FA_{0.83}Cs_{0.17}PbI_3$/PEIE/ZnO/ITO | 17.5 | 1282.7 | 50 |
| ITO/ZnO/PEIE/ $NH_2$-$PEG_4$-$NH_2$-$FAPbI_3$/TFB/$MoO_3$/Au | 19.2 | 360 | 51 |
| ITO/ZnO/PEIE/ AEAA-$FAPbI_3$/TFB/$MoO_3$/Au | 22.2 | 93 (at 85mA $cm^{-2}$) | 52 |
| ITO/ZnO/PEIE/3Cl-BA-$FAPbI_3$/TFB/$MoO_x$/Au | 16.6 | 300 (at 460mA $cm^{-2}$) | 53 |
| ITO/PEIE-ZnO/APS-$FAPbI_3$/TFB/$MoO_x$/Au | 19.2 | 240 (at 3.6V) | 54 |
| ITO/PEDOT:PSS/VB-FPND/ PEAI2-$FAPbI_3$ QDs/CN-T2T/LiF/Al | 15.4 | - | 55 |
| ITO/$SnO_2$/BDP/$FAPbI_3$+PCD/TPD/$MoO_3$/Au | 14 | 92 | This work |

**Aknowledgments**

This research is co-financed by Greece and the European Union (European Social Fund- ESF) through the Operational Programme «Human Resources Development, Education and Lifelong Learning» in the context of the project “Reinforcement of Postdoctoral Researchers - 2nd Cycle” (MIS-5033021), implemented by the State Scholarships Foundation (IKY).

**References**


1. Sutherland B R and Sargent E H 2016 Perovskite photonic source *Nat. Photonics* **10** 295–02.
2. Kovalenko M V, Protesescu L and Bodnarchuk M I 2017 Properties and potential optoelectronic applications of lead halide perovskite nanocrystals *Science* **358** 745–50.
3. Qiu W *et al* 2019 Mixed lead–tin halide perovskites for efficient and wavelength-tunable near-infrared light-emitting diodes. *Adv. Mater.* **31** 1806105.
4. Lai M L *et al* 2016 Tunable near-infrared luminescence in tin halide perovskite devices. *J. Phys. Chem. Lett.* **7** 2653–8.
5. Smith M D, Connor B A and Karunadasa H I 2019 Tuning the luminescence of layered halide perovskites *Chem. Rev.* **119** 3104–39.
6. Akkerman Q A, Rainò G, Kovalenko M V and Manna L 2018 Genesis, challenges and opportunities for colloidal lead halide perovskite nanocrystals *Nat. Mater.* **17** 394–05.
7. Xing G*et al* 2014 Low-temperature solution-processed wavelength-tunable perovskites for lasing *Nat. Mater.* **13** 476–80.
8. Tan Z.-K. *et al* 2014 Bright light-emitting diodes based on organometal halide perovskite *Nat. Nanotechnol.* **9** 687–92.
9. Cao Y *et al* 2018 Perovskite light-emitting diodes based on spontaneously formed submicrometre-scale structures *Nature* **562** 249–53.
10. Xu W *et al* 2019 Rational molecular passivation for high-performance perovskite light-emitting diodes *Nat. Photon.* **13** 418–24.
11. Wang H *et al* 2020 Perovskite-molecule composite thin films for efficient and stable light-emitting diodes *Nat. Commun.* **11** 891.
12. Jia Y.-H. *et al* 2020 Role of excess FAI in formation of high-efficiency $FAPbI_3$-based light-emitting diodes *Adv. Funct. Mater.* **30** 1906875.
13. Wang N. *et al* 2016 Perovskite light-emitting diodes based on solution-processed self-organized multiple quantum wells *Nat. Photonics* **10** 699–04.
14. Zhao B. *et al* 2018 High-efficiency perovskite-polymer bulk heterostructure light-emitting. *Nat. Photonics* **12** 783–9.
15. Hong W-L *et al* 2016 Efficient low-temperature solution-processed lead-free perovskite infrared light-emitting diodes *Adv. Mater.* **28** 8029–36.
16. Yang R *et al* 2018 Oriented quasi-2D perovskites for high performance optoelectronic devices *Adv. Mater.* **30** 1804771.
17. Tsai H *et al* 2018 Stable light-emitting diodes using phase-pure Ruddlesden–Popper layered perovskites *Adv. Mater.* **30** 1704217 (2018).

18. Giuri A *et al* 2018 Ultra-bright near-infrared perovskite light-emitting diodes with reduced efficiency roll-off *Sci. Rep.* **8** 15496.

19. Zhao X and Tan Z-K 2020 Large-area near-infrared perovskite light-emitting diodes *Nat. Photonics* **14** 215–18.

20. Protesescu L *et al* 2017 Dismantling the "red wall" of colloidal perovskites: highly luminescent formamidinium and formamidinium–cesium lead iodide nanocrystals. *ACS Nano* **11** 3119–34.

21. Tang H et al 2021 Carbon Quantum Dot-Passivated Perovskite/Carbon Electrodes for Stable Solar Cells. *ACS Appl. Nano Mater.* **4** 12, 13339–51.

22. Wu W Q, Huang F, Chen D, Cheng Y B and Caruso R A 2015 Thin films of dendritic anatase titania nanowires enable effective hole-blocking and efficient light-harvesting for high-performance mesoscopic perovskite solar cells *Adv. Funct. Mater.* **25** 3264–72.

23. Snaith H J and Ducati C 2010 $SnO_2$-based dye-sensitized hybrid solar cells exhibiting near unity absorbed photon-to-electron conversion efficiency *Nano Lett.* **10** 1259–65.

24. Wang H. 2018 Efficient perovskite light-emitting diodes based on a solution-processed tin dioxide electron transport layer *J. Mater. Chem. C* **6** 6996–02.

25. Gu F, Wang S F , Lü M K , Zhou G J, Xu D. and Yuan D. R. 2004 Photoluminescence properties of $SnO_2$ nanoparticles synthesized by sol−gel method *J. Phys. Chem. B* **108** 8119–23.

26. Vasilopoulou M *et al* 2021 Advances in solution-processed near-infrared light-emitting diodes *Nat. Photonics* **15** 656–69.

27. Tao P, Li Y, Rungta A, Viswanath A, Gao J, Benicewicz B C, Siegel R W and Schadler L S 2011 *J. Mater. Chem.* **21** 18623–9.

28. Dong Q, Shi Y, Wang K, Li Y, Wang S, Zhang H, Xing Y, Du Y, Bai X and Ma T 2015 Insight into perovskite solar cells based on $SnO_2$ compact electron-selective layer *J. Phys. Chem. C* **119** 10212–7.

29. Song J, Zheng E, Bian J, Wang X-F, Tian W, Sanehira Y and Miyasaka T. 2015 Low-temperature $SnO_2$-based electron selective contact for efficient and stable perovskite solar cells *J. Mater. Chem. A* **3** 10837–44.

30. Ladomenou K, Landrou G, Charalambidis G, Nikoloudakis E and Coutsolelos A G 2021 Carbon dots for photocatalytic $H_2$ production in aqueous media with molecular Co catalysts *Sustainable Energy Fuels* **5** 449-58.

31. Zhu S, Meng Q and Wang L 2013 Highly Photoluminescent Carbon Dots for Multicolor Patterning, Sensors, and Bioimaging *Angew. Chem.* **125** 4045–9.

32. Schneider J, Reckmeier C J, Xiong Y, von Seckendorff M, Susha A S, Kasák P and Rogach A L 2017 Molecular fluorescence in citric acid-based carbon dots *J. Phys. Chem. C* **121** 2014–22.

33. Song Y, Zhu S, Zhang S, Fu Y, Wang L, Zhao X and Yang B 2015 Investigation from chemical structure to photoluminescent mechanism: a type of carbon dots from the pyrolysis of citric acid and an amine *J. Mater. Chem. C* **3** 5976–84.

34. Zhu T *et al* 2018 A novel amphiphilic fluorescent probe BODIPY– O -CMC–cRGD as a biomarker and nanoparticle vector *RSC Advances* **8** (36) 20087–94.

35. Zhou Y *et al* 2012 A universal method to produce low-work function electrodes for organic electronics *Science* **336** 327–32.

36. Huang F, Wu H and Cao Y 2010 Water/alcohol soluble conjugated polymers as highly efficient electron transporting/injection layer in optoelectronic devices *Chem. Soc. Rev.* **39** 2500–21.

37. Zhong Z *et al* 2015 Hole-trapping effect of the aliphatic-amine based electron injection materials in the operation of OLEDs to facilitate the electron injection *Adv. Electron. Mater.* **1** 1400014.

38. Tumen-Ulzii G *et al* 2020 Hysteresis-less and stable perovskite solar cells with a self-assembled monolayer *Communications Materials* **1** 31.

39. Fakharuddin, A. *et al.* 2022 Perovskite light-emitting diodes. *Nat. Electron.* **5** 203–216.

40. Sealy C 2017 Nano-grained perovskite LEDs shine more brightly *NanoToday* **13** 5.

41. Nikolaidou K, Sarang S, Martin D, Tung V, Lu J Q and Ghosh S 2018 Tuning excitonic properties of pure and mixed halide perovskite thin films via interfacial engineering *Adv. Mater. Interfaces* 1800209.

42. Stathopoulos N A, Vasilopoulou M, Palilis L C, Georgiadou D G and Argitis P 2008 A combined experimental and simulation study on thickness dependence of the emission characteristics in multicolor single layer organic light-emitting diodes. *Appl. Phys. Lett.* **93** 083310.

43. Bae W K *et al.* 2013 Controlling the influence of Auger recombination on the performance of quantum-dot light-emitting diodes. *Nature Comm.* **4** 2661.

44. Kuang C, Hu Z, Yuan Z, Wen K, Ging J, Kobera L, Abbrent S, Brus J, Yin C, Wang H, Xu W, Wang J, Bai S and Gao F 2021 Critical role of additive-induced molecular interaction on the operational stability of perovskite light-emitting diodes *Joule* **5** 618–630.

45. Teng P, Reichert S, Xu W, Yang S-C, Fu F, Zou Y, Yin C, Bao C, Karlsson M, Liu X, Qin J, Yu T, Tress W, Yang Y, Sun B, Deibel C and Gao F 2021 Degradation and self-repairing in perovskite light-emitting diodes *Matter* **4** 3710–3724.

46. He Y, Yan J, Xu L, Zhang B, Cheng Q, Cao Y, Zhang J, Tao C, Wei Y, Wen K, Kuang Z, Chow G M, Shen Z, Peng Q, Huang W and Wang J 2021 Perovskite light-emitting diodes with near unit internal quantum efficiency at low temperatures *Adv. Mater.* **33** 2006302.

47. Ngai K H, Wei Q, Chen Z, Guo X, Qin M, Xie F, Chan C C S, Xing G, Lu X, Chen J, Wong K S, Xu J and Long M 2021 Enhanced electrochemical stability by alkyldiammonium in Dion–Jacobson perovskite toward ultrastable light- emitting diodes *Adv. Optical Mater.* **9** 2100243.

48. Jia Y, Yu H, Zhou Y, Li N, Guo Y, Xie F, Qin Z, Lu X and Zhao N 2021 Excess ion-induced efficiency roll-off in high-efficiency perovskite light-emitting diodes *ACS Appl. Mater. Interfaces* **13** 28546–28554.

49. Lee D-K, Shin Y, Jang H J, Lee J-H, Park K, Lee W, Yoo S, Lee J Y, Kim D, Lee J-W and Park N-G 2021 Nanocrystalline polymorphic energy funnels for efficient and stable perovskite light-emitting diodes *ACS Energy Lett.* **6** 1821–1830.

50. Guo Y, Apergi S, Li N, Chen M, Yin C, Yuan Z, Gao F, Xie F, Brocks G, Tao S and Zhao N, 2021 Phenylalkylammonium passivation enables perovskite light emitting diodes with record high-radiance operational lifetime: the chain length matters *Nat. Commun.* **12** 644.

51. Zou Y et al 2021 Manipulating crystallization dynamics through chelating molecules for bright perovskite emitters *Nat. Commun.* **12** 4831.

52. Zhu L *et al* 2021 Unveiling the additive-assisted oriented growth of perovskite crystallite for high performance lightemitting diodes *Nat. Commun.* **12** 5081.

53. Zhang H *et al* 2021 Low roll-off and high stable electroluminescence in three- dimensional $FAPbI_3$ perovskites with bifunctional-molecule additives *Nano Lett*. **21** 3738–3744.

54. Zhang J *et al* 2022 Sulfonic zwitterion for passivating deep and shallow level defects in perovskite light-emitting diodes *Adv. Funct. Mater*. 2111578.

55. Tseng Z-L, Chen L-C, Chao L-W, Tsai M-J, Luo D, Al Amin N R, Liu S-W and Wong K-T, 2022 Aggregation control, surface passivation, and optimization of device structure toward near-infrared perovskite quantum-dot light-emitting diodes with an EQE up to 15.4% *Adv. Mater*. 2109785.

56. Kahn SA *et al.* 2019. New physical insight into crystal structure, luminescence and optical properties of $YPO_4:Dy^{3+}\backslash Eu^{3+}\backslash Tb^{3+}$ single-phase white-light-emitting phosphors. *J. Alloys and Compounds* **817** 152687.

57. Kahn SA *et al.* 2021. Broad band white-light-emitting $Y_5Si_3O_{12}N:Ce^{3+}/Dy^{3+}$ Oxonitridosilicate phosphors for solid state lighting applications. *Journal of Luminescence* **229** 117687.